



Microstructure and microhardness of a novel TiZrAlV alloy by laser gas nitriding at different laser powers

Zhi-Hao Feng, Xin-Yang Sun, Peng-Biao Han, Hang Fu, Hui-Cong Dong, Shun Guo, Ru Su* , Jian-Hui Li* 

Received: 29 August 2019/Revised: 17 October 2019/Accepted: 12 December 2019/Published online: 3 February 2020
© The Nonferrous Metals Society of China and Springer-Verlag GmbH Germany, part of Springer Nature 2020

Abstract The Ti–20Zr–6.5Al–4V (T20Z, wt%) alloy surface was treated by the process of laser surface nitriding. The evolution of microstructures and microhardness has been investigated by changing the laser power parameter from 120 to 240 W. All laser-treated T20Z samples show two regions with distinctly different microstructural features, as compared with the untreated substrate: dense TiN dendrites and $(\alpha + \beta) - \text{Ti}$ (remelting zone, RMZ), nanoscale α laths doped with part of β phase (heat-affected zone, HAZ). The formation of TiN dendrites can be analyzed by a series of complex reactions during the process of melting and solidification. The increase in laser power results in the increase in content of TiN dendrite which is mainly due to the increase in energy input. In HAZ, the

self-quenching effect leads to the formation of nanoscale α laths and the residue of β phase. Microhardness profile of different regions was measured from the surface to the interior, and the highest microhardness was obtained (\sim HV 916.8) in the RMZ, as the laser power was set to 240 W. In the present study, we explained various microstructural characteristics induced by laser surface nitriding treatment.

Keywords TiZrAlV alloy; Laser surface nitriding; Microstructure; TiN dendrites; Microhardness

1 Introduction

Compared to other structural alloys, such as stainless steel and Co–Cr, titanium (Ti)-based alloys exhibit excellent properties like their exceptional corrosion resistance, satisfactory combination of strength and ductility, low density and high neutron absorption capability [1–3]. Based on these outstanding performances, there has been increasing interest in recent years on using Ti-based alloys in numerous applications, such as automotive, aerospace and nuclear industries [4–6]. However, surface failures due to low hardness, poor wear resistance and pitting corrosion restrict the utilization of Ti alloys in engineering fields [7, 8]. It is possible that tailoring the surface characteristics, such as microstructure, composition and mechanical properties via appropriate surface modification technique, can potentially minimize or even eliminate the surface failures due to low wear and poor corrosion resistance.

So far, several surface modification methods have been used for Ti alloys to improve their hardness, tribological and corrosion properties [9], such as thermal oxidation,

Z.-H. Feng, X.-Y. Sun, P.-B. Han, H. Fu, H.-C. Dong, R. Su*, J.-H. Li*

Hebei Key Laboratory of Material Near-net Forming Technology, Hebei University of Science and Technology, Shijiazhuang 050000, China
e-mail: sxru2008@163.com

J.-H. Li
e-mail: lijianhui_97@163.com

Z.-H. Feng, X.-Y. Sun, P.-B. Han, H. Fu, H.-C. Dong, R. Su, J.-H. Li

Hebei Engineering Laboratory of Aviation Lightweight Composite Materials and Processing Technology, Hebei University of Science and Technology, Shijiazhuang 050000, China

Z.-H. Feng, H.-C. Dong
State Key Laboratory of Metastable Materials Science and Technology, Yanshan University, Qinhuangdao 066004, China

S. Guo
School of Materials Science and Engineering, Jiangsu University, Zhenjiang 212013, China

TiN coating [10], nitrogen diffusion hardening [11], electron beam surface remelting or alloying [12, 13] and laser nitriding [14]. Usually, surface treatment processes based on laser energy input allow selective rapid melting, followed by rapid cooling (about 1×10^5 – 1×10^8 K·s⁻¹) due to high-speed heat extraction over the substrate metal [15]. Microstructures and related mechanical properties can be remarkably optimized during the instantaneous heating and cooling. Chai et al. [16] noted that the laser surface remelting could produce nanoscale α' plate structures which effectively improved the surface hardness of Zr702 alloy. Zhang et al. [13] characterized the surface hardness, and the results showed that corrosion resistance could be modified and the mechanisms are remarkable due to the formation of homogeneous fine α' martensitic protective layer by using low energy and high current pulsed electron beam technique. In particular, TiN has attracted considerable attention due to its high hardness and adhesion to the matrix. Dos Reis et al. [17] reported the microhardness of relatively pure TiN dendrites which was more than HV 1350 and was three times higher than that in the substrate for Ti–6Al–4V alloy. Obviously, the content and distribution of TiN phase determine the degree of surface performance optimization. Gas flow rate, laser power, scanning speed and laser beam diameter play an important role in regard to the depth of TiN layer, content and distribution of TiN phase [18, 19]. da Silva Briguente N et al. [20] studied the creep resistance of Ti–4Al–4V alloy after nitridation under different power conditions. The results show that laser surface nitridation can improve the creep resistance of the material. However, due to the increase in the thickness of the nitrided layer under high-power conditions, the hardness value of the surface layer is increased, and the creep resistance of the material is lowered. Katahira et al. [21] prepared a TiN coating on the surface of titanium alloy under different power conditions. The surface roughness and thickness of the nitrided layer increased with the increase in power, and the combination of power parameters with the best surface roughness and nitriding effect was obtained through research. In addition, it is worth noting that laser surface treatment induces stress, which may lead to cracking for the treated materials. Mridha and Baker [22] confirmed that the type of stress due to phase transformation during rapid heating and cooling depends on several parameters including heat input (either by decreasing the scanning speed or by increasing the laser power) and gas flow rate. The appearance of cracks has a negative effect on the surface characteristics of materials. Therefore, the optimization of laser processing parameters should be concerned in order to obtain excellent microstructures and related properties.

Ti–20Zr–6.5Al–4V (T20Z, wt%) alloy corresponds to a variant of the Ti–6Al–4V alloy [23]. The development of

T20Z represents mechanical performance improvement for parts previously. However, the hardness is low and pitting corrosion also occurs frequently on the surface of T20Z [24]. In the present work, we had treated the surface of T20Z by laser surface nitriding and studied the effects of laser powers on microstructure, phase composition and microhardness. The aim was to use laser surface nitriding in the design of experiment to find suitable processing parameters which produce deep nitrided layers with a high surface hardness.

2 Experimental

2.1 Material preparation

A newly developed T20Z alloy was used as the substrate material. The nominal chemical composition (wt%) of the alloy is listed as follows: 20 Zr, 6.5 Al, 4 V and balanced Ti. In order to eliminate the residual stress and to ensure more uniform composition, T20Z alloy was heat-treated at 900 °C for 90 min in a tubular vacuum heat treatment furnace with protective argon environment and followed by furnace cooling. After that, the alloy samples were cut into 60 mm × 10 mm × 10 mm pieces. The alloy surface was polished carefully and then chemically cleaned by acetone to eliminate the surface contamination.

2.2 Laser surface nitriding (LSN)

A pulsed 600 W lamp-pumped CW Nd: YAG laser device was used to irradiate the surface of T20Z samples. Powers of the laser source were set into 120, 180 and 240 W. Laser scanning speed and laser beam diameter parameters were identified as 10 mm·s⁻¹ and 1 mm. The melted area was protected with a continuous flow of nitrogen gas (10 L·min⁻¹). The schematic diagram of the laser device and the trajectory of the laser beam on the surface of the sample are shown in Fig. 1.

2.3 Characterizations

The phases of the specimens were confirmed by using the conventional X-ray powder diffraction (XRD) with Cu $\kappa\alpha$ radiation (D/max-2500/PC). The influence of the process parameters on the microstructure of the nitrided surface was studied via scanning electron microscopy (SEM, Hitachi, S3400N) and transmission electron microscopy (TEM, JEOLJEM-2010). Microstructures of the samples were analyzed by using a Hitachi S4800 field-emission scanning electron microscope (FESEM) coupled with an energy-dispersive X-ray spectrometer (EDS). Microhardness for the LSN-treated samples was measured by Vickers

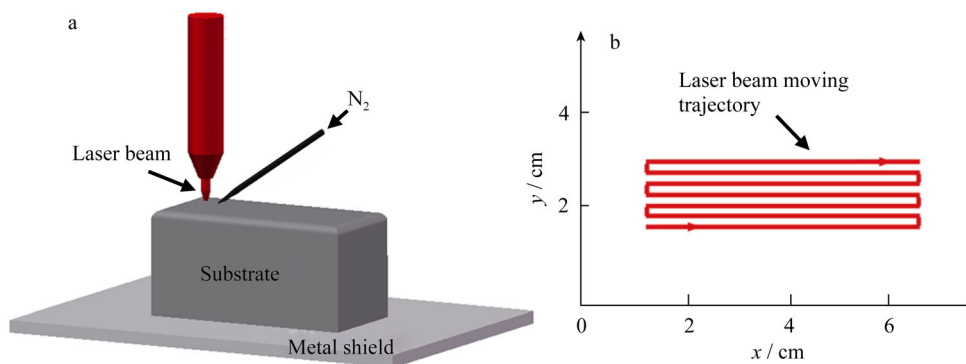


Fig. 1 **a** Schematic diagram of laser device and **b** trajectory of laser beam on surface of sample

hardness tester (HVS-1000) with a load of 0.98 N for 10 s. The tester could accurately locate the position (coordinate) of each indentation that allowed correlation with the specific microstructures. To avoid any inconsistencies, all the microhardness tests were performed at least three times on each nitrided specimen under different parameters.

3 Results and discussion

Figure 2 shows XRD patterns of the original T20Z specimen (before LSN treatment). The main peaks of the α phase and the β phase at $2\theta \approx 55.6^\circ$ indicate that the alloy is two-phase structure composed of α and β . XRD data revealed that the contents of α and β phases in the matrix can be calculated as 88.2% and 11.8%, respectively, by using previously described method [25–27]. To identify the distribution of α and β phases of original T20Z specimen, SEM image and relevant EDS analysis are shown in Fig. 3. The analyzed regions are indicated with red spots in Fig. 3a, and the EDS analysis is shown in Fig. 3b, c. The results show that the content of Al is higher in Spot 1 than in Spot 2, whereas the contents of V and Zr are lower. Previous studies have confirmed that V and Zr are β

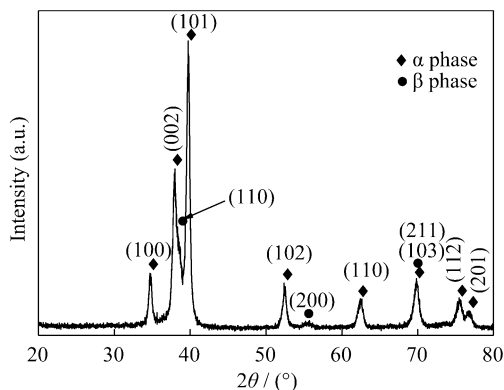


Fig. 2 XRD patterns of annealed T20Z sample (before laser surface nitriding treatment)

stabilizing elements and Al is an α stabilizing element [23, 28, 29]. Therefore, the phase distribution can be mediated by the difference in the content of solid solution elements. Combined with XRD results, EDS findings determine that the lamella microstructures are α phase regions and that the light-gray microstructures are β phase.

Figure 4 depicts the cross-sectional views of specimen microstructures at different laser powers. The three zones (remelting zone: RMZ, heat-affected zone: HAZ and substrate zone: SZ) with distinct morphologies can be easily distinguished from the low magnification images, as indicated by red dashed lines in Fig. 4a–c. The average thickness of RMZ and HAZ at different laser powers, as shown in Fig. 4d, clearly indicates that the increase in laser power leads to the increase in the thickness of RMZ and HAZ. The average thickness is approximately 403 and 561 μm for RMZ and HAZ, respectively, with a laser power of 120 W. When the laser power increases to 240 W, the average thickness of RMZ and HAZ dramatically increases to 519 and 934 μm , respectively. The observed variations in the RMZ thickness can be explained on the variations of melt pool depth as a function of laser energy input [30–32]. Combining with the previous studies, the line energy density (E_{line}) can be measured from the average applied energy per line length of material during the surface scanning [33–35]:

$$E_{\text{line}} = \frac{P_{\text{beam}}}{V_{\text{scan}}} \quad (1)$$

where P_{beam} is the laser power and V_{scan} is the laser beam scanning speed. In the present study, $V_{\text{scan}} = 10 \text{ mm}\cdot\text{s}^{-1}$. Obviously, E_{line} increases with the increase of P_{beam} . As the laser power increases, a large amount of liquid phase can be produced, eventually leading to a deeper melt pool. Similarly, a higher line energy density initiated at a higher laser power can allow more energy to be transferred through the bottom of the melt pool to HAZ. The results indicate that a higher value of average thickness of HAZ could be achieved with a laser power of 240 W.

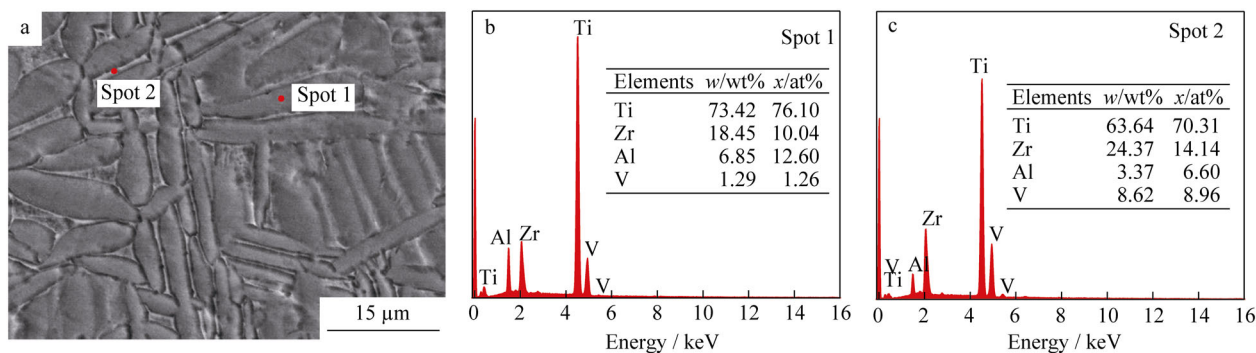


Fig. 3 a SEM image annealed T20Z sample and corresponding EDS point analysis results of **b** Spot 1 and **c** Spot 2 indicated in SEM image

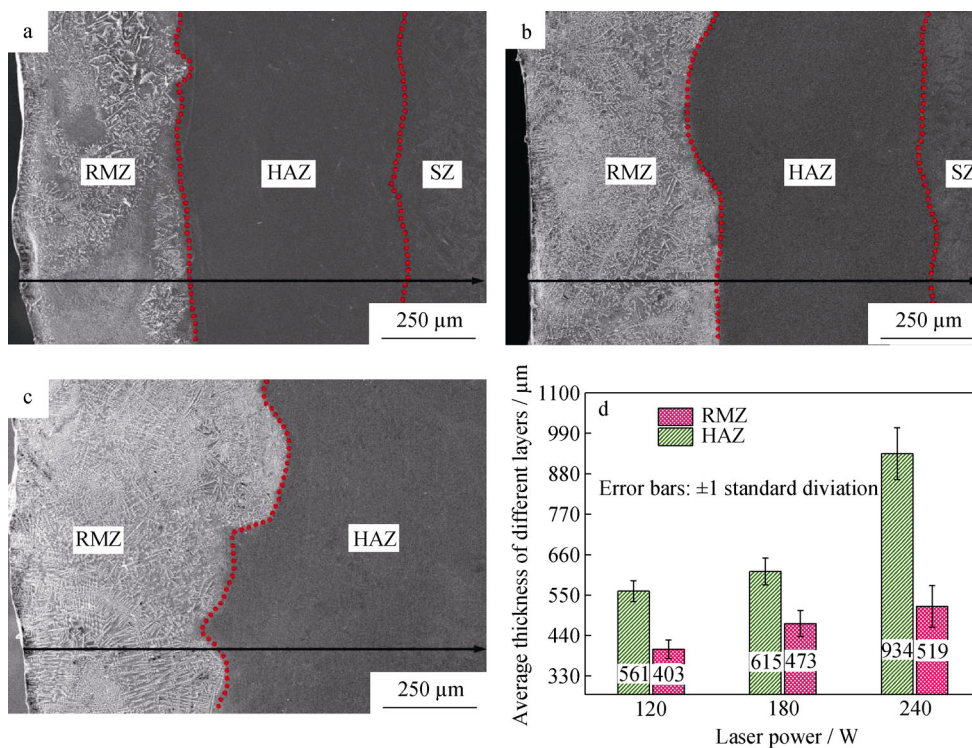


Fig. 4 Cross-sectional views of specimen microstructures at various laser scanning speeds: **a** 120 W, **b** 180 W, **c** 240 W and **d** average thickness of RMZ and HAZ at different laser powers

Chikarakara et al. [31] have summarized that an increase in the laser energy inputs could result in a raise in processing depth of the laser-melted Ti–6Al–4V alloy, which is coincident with the present study.

The results of XRD analyses are performed to determine the phase constitution of the laser surface nitrided specimens with different laser power inputs, as shown in Fig. 5. XRD spectra of RMZ and HAZ at different laser power inputs indicate the formation of α and β phases. Although α and β phases are dominant for all three processing conditions, it should be noted that the diffraction peaks of the TiN phase ($2\theta \approx 36.7^\circ$ and 42.6°) in the RMZ region exhibit face-centered cubic structure, which systematically increased with the increase in laser power. The increase in

the height of diffraction peaks of TiN phase can be justified based on the fact that with the increase in laser energy density, more energy input is allowed for nitrogen diffusion into the T20Z substrate, thereby forming more TiN phases in RMZ. Abboud [36] showed a similar result of TiN, but the angles were slightly different. Table 1 lists the 2θ angles and lattice constants of TiN phase in the present study and also compared the values with the reported Ti–6Al–4V alloy in Ref. [36]. The article reported that the diffraction angles of TiN peaks on (111) and (200) planes are 37.1° and 42.9° , respectively. In addition, the lattice parameter obtained in the present study is 0.476 nm, which is higher than the reported value of TiN (0.4192 nm). The

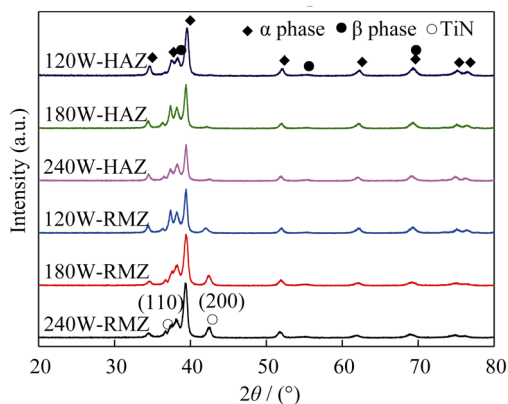


Fig. 5 XRD patterns of laser surface nitrided specimens at different laser powers

Table 1 2θ angles and lattice constants of TiN phase in the present study and reported Ti–6Al–4V alloy in Ref [36]

Alloy	$2\theta/(\circ)$	(hkl)	Lattice parameter/nm
T20Z	36.7	(111)	0.4276
	42.6	(200)	
Ti–6Al–4V [36]	37.1	(111)	0.4192
	42.9	(200)	

variation of lattice parameters is often based on the composition of alloys. It is well known that the chemical properties of Zr and Ti are similar, and both belong to the IVB group in the periodic table. In addition, the Ti–Zr system forms a completely solid solution [23]. Owing to the larger atomic radius of Zr (0.162 nm) than Ti (0.147 nm), the accession of Zr results in lattice distortion that causes the increase in lattice parameters of TiN phase. These distortions cause the XRD peaks to shift gradually toward the low-angle orientation.

Figure 6 shows RMZ micrographs of laser beam nitrided T20Z samples at different laser powers. The samples show a mixed structure of dendrites and lath structure, as shown in Fig. 6a–c. To determine the composition of dendritic region and lath-like region, EDS analysis was performed at Spots 1 and 2, and the relevant results are shown in Fig. 6d, e. EDS results at Spot 1 show that the atomic ratio of N to Ti is close to 1:1, which indicates the formation of TiN dendrites. In contrast, the composition at Spot 2 indicates that there is no N in the lath-like region. Combined with the results of XRD, it can be confirmed as a mixed structure composed of α and β .

The formation of TiN dendrites can be analyzed by melting and solidification processes. During surface melting in nitrogen environment, a large quantity of nitrogen gas entered into the melt pools by adsorption and

dissolution. Subsequently, TiN phase can be formed through a series of reactions. The mechanism of TiN formation during laser melting in nitrogen environment can be explained by the following reactions [37]:

Surface adsorption:



Dissociation (nitrogen decomposition):



Nitrogen diffusion:



TiN-phase precipitation:



Melt solidification:



where square bracket ([]) refers to a liquid solution and (N) represents N in the T20Z alloy surface. It is clear that a series of complex reactions occurs successively during melting and solidification processes. TiN can nucleate after N_2 subjected to adsorption, decomposition and diffusion processes in the melt pools. The nucleation of TiN decreases to liquidus, which leads to constitutional supercooling and dendrite growth. The remaining components form mixed phases of α and β during melt solidification.

Laser process parameters have a very important effect on the content of TiN dendrites [38]. The present research showed that more TiN dendrites may be produced by increasing the laser power. Figure 7 depicts the statistics of content of TiN dendrites as a function of laser power. In order to obtain accurate data, the study calculated the proportion of dendrites in the RMZ of five samples by using the area image analysis volume fraction measurement method [39]. The maximum content achieved by 86.7 vol% after the process of laser nitriding with a laser power of 240 W, while the minimum of 49.2 vol% was produced at 120 W. The increase in the TiN content with the increase in laser power can be attributed to a high level of absorbed energy. In addition, by increasing the laser power, the liquid residence time increased. As a result, N_2 could decompose and diffuse sufficiently in the melt pool and eventually form more TiN dendrites.

Figure 8 shows TEM images of HAZ at various laser powers which can be used to investigate the specific distribution and morphology of α and β phases. The gray region indicates α phase, and the black region represents β phase. Most of α grains exhibit a distinct basket-like structure although exposed to different scanning speeds. We have found two phenomena as shown in Fig. 8: One is the evolution of β phase content and the other is the size

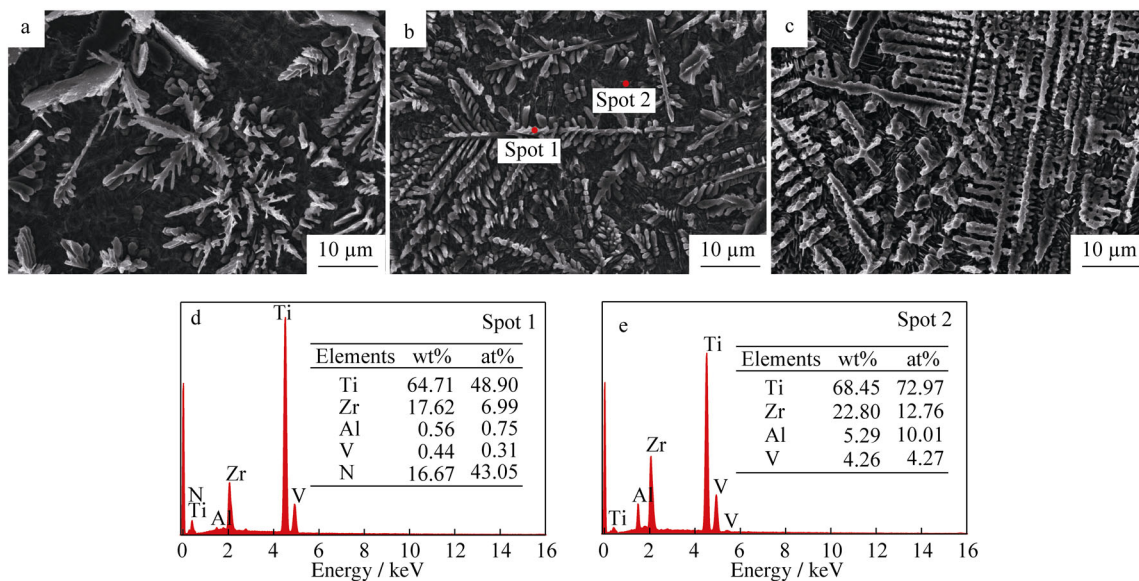


Fig. 6 RMZ images (SEM) of laser surface nitrided T20Z samples at different laser powers: **a** 120 W, **b** 180 W, **c** 240 W and EDS point analysis results of **d** Spot 1 and **e** Spot 2 indicated in SEM image

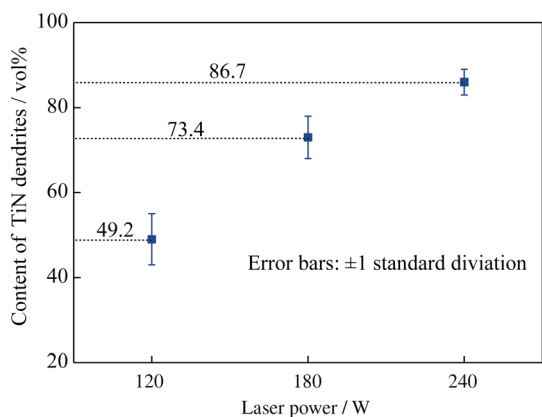


Fig. 7 Statistics of the volume fraction of TiN dendrites as a function of laser power

change of α laths width. The average grain size of the HAZ was measured according to the semiautomated image method (ASTM: E1382-97(2015)). In order to obtain accurate data, three-to-five samples were measured in this study. Combining with the current XRD results and previous studies [25–27], the β phase content can be estimated and the results are listed in Table 2. The β phase content decreases gradually from 20.38 vol% to 13.11 vol% with the increase in laser power from 120 to 240 W. In addition, the average width of α laths increases from 28.4 to 46.1 nm under different laser powers.

In HAZ, the T20Z sample has only undergone heating and cooling processes without involving the melting. Therefore, phase composition and tissue morphology are only related to the absorption and dissipation of energy during heating or cooling. It is well known that the

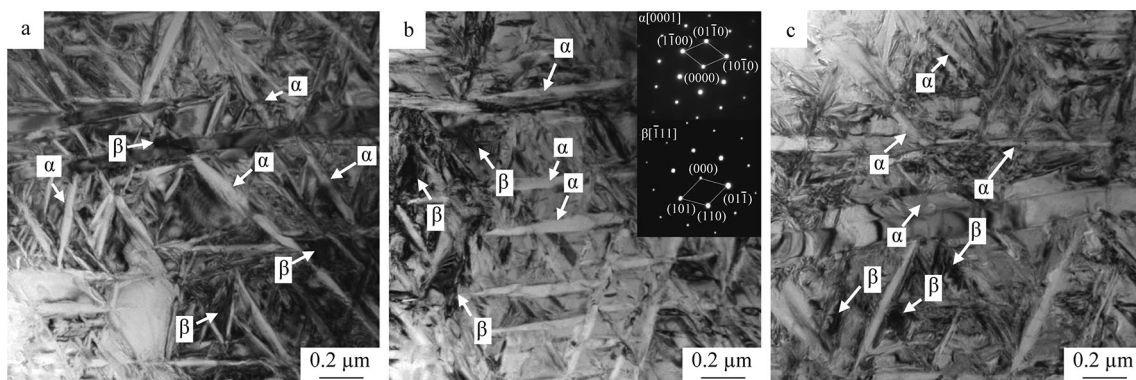


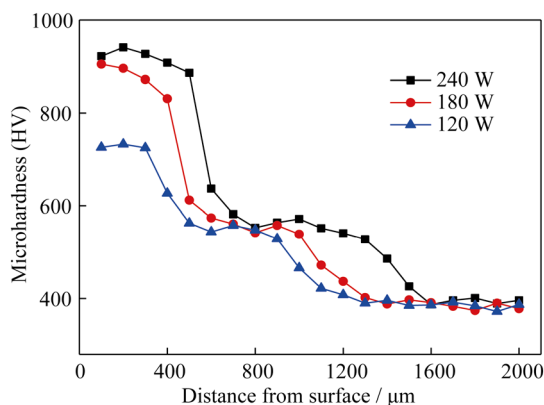
Fig. 8 TEM images of HAZ at various laser powers: **a** 120 W, **b** 180 W and **c** 240 W

Table 2 Content of β phase and average width of α laths in HAZ at different laser powers

Laser powers/ W	Content of β phase/ vol%	Average width of α laths/ nm
120	20.38 ± 5	28.4 ± 11.0
180	15.86 ± 3	37.3 ± 14.0
240	13.11 ± 2	46.1 ± 17.0

generation of basket-like α structure in Ti alloys is related to the solid-state phase transformation, generally during rapid β cooling [40, 41]. When the T20Z sample is irradiated by laser beam, HAZ will be rapidly heated with the peak temperature easily exceeding β transition point. When the laser energy stops, the energy absorbed by HAZ will transfer rapidly to the surrounding environment by diffusion. Generally, the process is very short and is called self-quenching effect [16]. Therefore, the basket-like α laths were transformed from the original β , and the residual β phase was obtained after self-quenching. In any case, the maximum energy can be absorbed by the sample when the laser power is 240 W. Furthermore, the heat of the HAZ needs to take long time to diffuse to the surface of the sample during subsequent cooling due to the hindrance caused by deeper RMZ. In comparison, the slower cooling rate promotes the solid-state phase transformation from β to α and further supports the growth of α laths. Therefore, the lowest β phase content and the widest α lath can be obtained in the T20Z sample when the laser power is set to 240 W.

The microhardness profile of different regions in the LSN-treated samples is measured and shown in Fig. 9 and Table 3. The microhardness measuring path has been indicated by the long arrow in Fig. 4, indicating their correspondence to specific zones. Based on the experimental data, it can be concluded that the microhardness

**Fig. 9** Microhardness profile along depth from surface of laser surface nitrided T20Z samples**Table 3** Average microhardness values of different regions in laser surface nitrided T20Z samples (HV)

Laser powers/W	RMZ	HAZ	SZ
120	702.8 ± 18.0	548.7 ± 19.0	386.2 ± 10.0
180	876.0 ± 23.0	551.1 ± 21.0	385.3 ± 14.0
240	916.8 ± 19.0	557.2 ± 14.0	391.2 ± 17.0

values can be directly affected by laser surface nitriding parameters and specific regions.

Taking the T20Z sample with a laser power of 240 W as an example, an average microhardness value of HV 916.8 can be determined for RMZ, which begins from the surface to the depth of about 519 μm . HAZ is found to be much softer than RMZ and the average microhardness value obtained for this region is HV 557.2. However, those values in RMZ and HAZ are obviously higher than that in SZ (about HV 391.2). Jing et al. [24] reported microhardness value of T20Z alloy was about HV 380 after the annealing process at 1050 $^{\circ}\text{C}$, which is similar to the value of SZ obtained in the present study. The dense TiN dendrite in RMZ produced a greater hardness, as compared with the other regions in the absence of TiN dendrites (HAZ and SZ). Dos Reis et al. [17] reported that the microhardness of relatively pure TiN dendrites was HV 1350. However, the microhardness value in RMZ is smaller than that of pure TiN and the reason could be the formation of a small amount of α and β grains in RMZ. Abboud et al. [38] also reported that the microhardness of nitrided layer decreased with the increase of α' -Ti matrix content by following the laser gas nitriding of Ti-6Al-4 V. A relatively large hardness variation of HAZ and SZ can be attributed to the size of α laths. The average width of α laths with 240 W laser power is about 46.1 nm, as shown in Table 3, which is over 40 times smaller than that in the SZ. The decrease in the size of α laths reduced the distance of dislocation in the grain boundary, resulting in an increase in the number of piling up dislocations. Furthermore, reducing the grain size increases the density of grain boundary at the same cross-sectional area. Consequently, the movement of the dislocation obstacle increases. The above two reasons lead to the increase in microhardness in HAZ.

In addition to the variations between different regions under the same processing conditions discussed above, the microhardness of T20Z samples at different laser powers was also analyzed briefly. Figure 9 indicates that a higher hardness can be obtained in RMZ using higher laser power. Combining the results of phase composition (Fig. 5) and microstructure (Figs. 6, 7), the higher laser energy input actually increases the dissolution of nitrogen and the subsequent increase in the concentration of TiN dendrites in

the melt, resulting in higher hardness values. Several other studies have also confirmed that the microhardness in nitrided layer increases with the increased concentration of TiN [22, 42]. In addition, the average width of α laths in HAZ increases slightly with the increase in laser power from 120 to 240 W. Based on the fine grain strengthening theory, the microhardness of HAZ should increase gradually with the decrease in laser power. In any case, the expected results were not observed and replaced by similar hardness values (as shown in Fig. 9 and Table 3). As previously analyzed, the content of β phase decreases gradually with the increase in laser power from 120 to 240 W. The families of slip planes and slip directions in the β phase with body-centered cubic structure were $\{110\}$ and $\langle 111 \rangle$, respectively, which could be combined into a higher number of slip systems. Therefore, the dislocations produced during the deformation of alloys containing the β phase could easily perform the slip motion. Clearly, similar microhardness values in the HAZ may originate from the size of α laths and the content of β phase.

4 Conclusion

After the laser surface nitriding treatments at different laser powers, two regions with distinctly different microstructural features compared with the substrate are presented: RMZ—a mixed structure of TiN dendrites and $(\alpha + \beta) - \text{Ti}$, HAZ—fine α laths and residual β phase. The maximum TiN dendrites content of 86.7 vol% can be obtained at laser power of 240 W. The increase in TiN content with the increase in laser power may be attributed to higher absorption energy. In HAZ, β phase content decreases gradually but the average α laths width increases as the laser power increases from 120 to 240 W. These two phenomena can be explained by self-quenching effect. The high value ($\sim \text{HV } 916.8$) of microhardness can be obtained in RMZ with a laser power of 240 W which is believed to arise from the dense TiN dendrites. Besides, similar values of microhardness in HAZ at different laser parameters can be obtained which is related to the width of α laths and the content of β phase.

Acknowledgements This study was financially supported by the Youth Top Talents Research Project of Hebei Provincial Education Department China (No. BJ2018052), the Natural Science Foundation of Hebei Province of China (Nos. E2019208205 and E2018208126), the National Natural Science Foundation of China (No. 51701064), the Science and Technology on Plasma Dynamics Laboratory Fund Project (No. 614220206021806), the Key Research and Development Program of Hebei Province (No. 19211016D) and the Open Foundation of State Key Laboratory of Metastable Materials Science and Technology (Nos. 201804 and 201812).

References

- [1] Li W, Liu J, Zhou Y, Li S, Wen S, Wei Q, Yan C, Shi Y. Effect of laser scanning speed on a Ti–45Al–2Cr–5Nb alloy processed by selective laser melting: microstructure, phase and mechanical properties. *J Alloy Compd.* 2016;688:626.
- [2] Yang Y, Chen RR, Fang HZ, Guo JJ, Ding HS, Su YQ, Fu HZ. Improving microstructure and mechanical properties of alloy Ti43Al5Nb0.1B by addition of Fe. *Rare Met.* 2019;38(11):1024.
- [3] MacLeod SG, Tegner BE, Cynn H, Evans WJ, Proctor JE, McMahon MI, Ackland GJ. Experimental and theoretical study of Ti–6Al–4V to 220 GPa. *Phys Rev B.* 2012;85(22):224202.
- [4] Boyer RR, Briggs RD. The use of β titanium alloys in the aerospace industry. *J Mater Eng Perform.* 2005;14(6):681.
- [5] Akahori T, Niinomi M, Fukui H, Ogawa M, Toda H. Improvement in fatigue characteristics of newly developed beta type titanium alloy for biomedical applications by thermo-mechanical treatments. *Mater Sci Eng, C.* 2005;25(3):248.
- [6] Ikeda M, Komatsu SY, Sowa I, Niinomi M. Aging behavior of the Ti–29Nb–13Ta–4.6Zr new beta alloy for medical implants. *Metall Mater Trans.* 2002;33(3):487.
- [7] Vaithilingam J, Goodridge RD, Hague RJ, Christie SD, Edmondson S. The effect of laser remelting on the surface chemistry of Ti6Al4 V components fabricated by selective laser melting. *J Mater Process Technol.* 2016;232:1.
- [8] Meier H, Haberland C. Experimental studies on selective laser melting of metallic parts. *Materialwiss Werkstofftech.* 2008;39(9):665.
- [9] Jin L, Zhou HB, Huang ZZ, Zhang T, Zhi X. Preparing and anticorrosion properties of Fe and Al based amorphous coatings. *Rare Met.* 2018;38(6):283.
- [10] Wang Y, Qian Z, Li XY, Tandon KN. Sliding wear properties of TiAl alloys with/without TiN coatings. *Surf Coat Technol.* 1997;91(1–2):37.
- [11] Rodriguez D, Gil FJ, Planell JA. Wear resistance of the nitrogen diffusion hardening of the Ti–6Al–4 V alloy. *J Biomech.* 1998;1001(31):49.
- [12] Proskurovsky DI, Rotshtein VP, Ozur GE, Ivanov YF, Markov AB. Physical foundations for surface treatment of materials with low energy, high current electron beams. *Surf Coat Technol.* 2000;125(1–3):49.
- [13] Zhang XD, Hao SZ, Li XN, Dong C, Grosdidier T. Surface modification of pure titanium by pulsed electron beam. *Appl Surf Sci.* 2011;257(13):5899.
- [14] Sathish S, Geetha M, Pandey ND, Richard C, Asokamani R. Studies on the corrosion and wear behavior of the laser nitrided biomedical titanium and its alloys. *Mater Sci Eng, C.* 2010;30(3):376.
- [15] Yao Y, Li X, Wang YY, Zhao W, Li G, Liu RP. Microstructural evolution and mechanical properties of Ti–Zr beta titanium alloy after laser surface remelting. *J Alloy Compd.* 2014;583:43.
- [16] Chai L, Chen B, Wang S, Guo N, Huang C, Zhou Z, Huang W. Microstructural changes of Zr702 induced by pulsed laser surface treatment. *Appl Surf Sci.* 2016;364:61.
- [17] dos Reis AG, Reis DAP, de Moura Neto C, Barboza MJR, Oñoro J. Creep behavior and surface characterization of a laser surface nitrided Ti–6Al–4V alloy. *Mater Sci Eng, A.* 2013;577:48.
- [18] Mahamood RM, Akinlabi ET, Akinlabi S. Laser power and scanning speed influence on the mechanical property of laser metal deposited titanium-alloy. *Lasers Manuf Mat Process.* 2015;2(1):43.
- [19] Dahotre SN, Vora HD, Pavani K, Banerjee R. An integrated experimental and computational approach to laser surface nitriding of Ti–6Al–4V. *Appl Surf Sci.* 2013;271:141.

- [20] da Silva Briguente N, Aparecida L, Oñoro J. The influence of laser nitriding on creep behavior of Ti–4Al–4V alloy with widmanstätten microstructure. *Metals*. 2019;9(2):236.
- [21] Katahira K, Tanida Y, Takesue S. Rapid surface nitriding of titanium alloy by a nanosecond fiber laser under atmospheric conditions. *CIRP Ann*. 2018;67(1):563.
- [22] Mridha S, Baker TN. Effects of nitrogen gas flow rates on the microstructure and properties of laser-nitrided IMI318 titanium alloy (Ti–4V–6Al). *J Mater Process Technol*. 1998;77(1–3):115.
- [23] Jing R, Liang SX, Liu CY, Ma MZ, Zhang XY, Liu RP. Structure and mechanical properties of Ti–6Al–4V alloy after zirconium addition. *Mater Sci Eng, A*. 2012;552:295.
- [24] Jing R, Liang SX, Liu CY, Ma MZ, Liu RP. Effect of the annealing temperature on the microstructural evolution and mechanical properties of TiZrAlV alloy. *Mater Des*. 2013;52:981.
- [25] Liang SX, Yin LX, Liu XY, Jing R, Zhou YK, Ma MZ, Liu RP. Effects of annealing treatments on microstructure and mechanical properties of the Zr345Ti35Al33V alloy. *Mater Sci Eng, A*. 2013;582:374.
- [26] Zhang B, Zhang X, Zhang XY, Jia YZ, Ma MZ, Liu RP, Jing Q. Effects of microstructure on the mechanical properties of a high-strength Ti20Zr6.5Al4V alloy. *J Alloy Compd*. 2018;735:2133.
- [27] Haghighi SE, Liu YJ, Cao GH, Zhang LC. Influence of Nb on the β/α martensitic phase transformation and properties of the newly designed Ti–Fe–Nb alloys. *Mater Sci Eng, C*. 2016;60:503.
- [28] Jiang XJ, Jing R, Liu CY, Ma MZ, Liu RP. Structure and mechanical properties of TiZr binary alloy after Al addition. *Mater Sci Eng, A*. 2013;586:301.
- [29] Dong HC, Feng ZH, Ma MZ, Zhang XY, Liu RP. Optimization of phase composition and mechanical properties in Zr alloys by micro-alloying. *Mater Lett*. 2017;202:25.
- [30] Balla VK, Soderlind J, Bose S, Bandyopadhyay A. Microstructure, mechanical and wear properties of laser surface melted Ti6Al4V alloy. *J Mech Behav Biomed Mater*. 2014;32:335.
- [31] Chikarakara E, Naher S, Brabazon D. High speed laser surface modification of Ti–6Al–4V. *Surf Coat Technol*. 2012;206(14):3223.
- [32] Singh R, Kurella A, Dahotre NB. Laser surface modification of Ti–6Al–4V: wear and corrosion characterization in simulated biofluid. *J Biomater Appl*. 2006;21(1):49.
- [33] Chen Z, Liu Y, Wu H, Zhang W, Guo W, Tang H, Liu N. Microstructures and wear properties of surface treated Ti–36Nb–2Ta–3Zr–0.35O alloy by electron beam melting (EBM). *Appl Surf Sci*. 2015;357:2347.
- [34] Juechter V, Scharowsky T, Singer RF, Körner C. Processing window and evaporation phenomena for Ti–6Al–4V produced by selective electron beam melting. *Acta Mater*. 2014;76:252.
- [35] Gustmann T, Schwab H, Kühn U, Pauly S. Selective laser remelting of an additively manufactured Cu–Al–Ni–Mn shape-memory alloy. *Mater Des*. 2018;153:129.
- [36] Abboud JH. Effect of processing parameters on titanium nitrided surface layers produced by laser gas nitriding. *Surf Coat Technol*. 2013;214:19.
- [37] Labudovic M, Kovacevic R, Kmecko I, Khan TI, Bleic D, Bleic Z. Mechanism of surface modification of the Ti–6Al–4V alloy using a gas tungsten arc heat source. *Metall Mater Trans A*. 1999;30(6):1597.
- [38] Abboud JH, Fidel AF, Benyounis KY. Surface nitriding of Ti–6Al–4V alloy with a high power CO₂ laser. *Opt Laser Technol*. 2008;40(2):405.
- [39] Shi D, Winslow D. Accuracy of a volume fraction measurement using areal image analysis. *J Test Eval*. 1991;19(3):210–3.
- [40] Wanying L, Yuanhua L, Yuhai C, Taihe S, Singh A. Effect of different heat treatments on microstructure and mechanical properties of Ti6Al4V titanium alloy. *Rare Met Mater Eng*. 2017;46(3):634.
- [41] Li H, Zhao Z, Guo H, Yao Z, Ning Y, Miao X, Ge M. Effect of initial alpha lamellar thickness on deformation behavior of a near- α high-temperature alloy during thermomechanical processing. *Mater Sci Eng, A*. 2017;682:345.
- [42] Draper CW, Mazzoldi P. *Laser Surface Treatment of Metals*. Dordrecht: Springer; 2012. 213.